

# Optimal Taylor-Couette flow: radius ratio dependence

RODOLFO OSTILLA M Ó NICO<sup>1</sup>,  
SANDER G. HUISMAN<sup>1</sup>,  
TIM J. G. JANNINK<sup>1</sup>, DENNIS P. M. VAN GILS<sup>1</sup>,  
ROBERTO VERZICCO<sup>2,1</sup>,  
SIEGFRIED GROSSMANN<sup>3</sup>, CHAO SUN<sup>1</sup>,  
AND DETLEF LOHSE<sup>1</sup>

<sup>1</sup>Physics of Fluids, Mesa+ Institute, University of Twente, P.O. Box 217, 7500 AE Enschede, The Netherlands

<sup>2</sup>Dipartimento di Ingegneria Meccanica, University of Rome “Tor Vergata”, Via del Politecnico 1, Roma 00133, Italy

<sup>3</sup>Department of Physics, University of Marburg, Renthof 6, D-35032 Marburg, Germany

(Received 12 April 2019)

Taylor–Couette flow with independently rotating inner (i) & outer (o) cylinders is explored numerically and experimentally to determine the effects of the radius ratio  $\eta$  on the system response. Numerical simulations reach Reynolds numbers of up to  $Re_i = 9.5 \cdot 10^3$  and  $Re_o = 5 \cdot 10^3$ , corresponding to Taylor numbers of up to  $Ta = 10^8$  for four different radius ratios  $\eta = r_i/r_o$  between 0.5 and 0.909. The experiments, performed in the Twente Turbulent Taylor–Couette ( $T^3C$ ) setup, reach Reynolds numbers of up to  $Re_i = 2 \cdot 10^6$  and  $Re_o = 1.5 \cdot 10^6$ , corresponding to  $Ta = 5 \cdot 10^{12}$  for  $\eta = 0.714 - 0.909$ . Effective scaling laws for the torque  $J^\omega(Ta)$  are found, which for sufficiently large driving  $Ta$  are independent of the radius ratio  $\eta$ . As previously reported for  $\eta = 0.714$ , optimum transport at a non-zero Rossby number  $Ro = r_i|\omega_i - \omega_o|/[2(r_o - r_i)\omega_o]$  is found in both experiments and numerics.  $Ro_{opt}$  is found to depend on the radius ratio and the driving of the system. At a driving of about  $Ta \sim 10^{10}$ ,  $Ro_{opt}$  saturates to an asymptotic  $\eta$ -dependent value. Theoretical predictions for the asymptotic value of  $Ro_{opt}$  are compared to the experimental results, and found to differ notably. Furthermore, the local angular velocity profiles from experiments and numerics are compared, and a link between a flat bulk profile and optimum transport for all radius ratios is reported.

**Key words:**

## 1. Introduction

Taylor-Couette (TC) flow consists of the flow between two coaxial cylinders which are independently rotating. A schematic drawing of the system can be seen in Fig. 1. The rotation difference between the cylinder shears the flow thus driving the system. This rotation difference has been traditionally expressed by two Reynolds numbers, the inner cylinder  $Re_i = r_i\omega_i d/\nu$ , and the outer cylinder  $Re_o = r_o\omega_o d/\nu$  Reynolds numbers, where  $r_i$  and  $r_o$  are the radii of the inner and outer cylinder, respectively,  $\omega_i$  and  $\omega_o$  the inner and outer cylinder angular velocity,  $d = r_o - r_i$  the gap width, and  $\nu$  the kinematic viscosity.

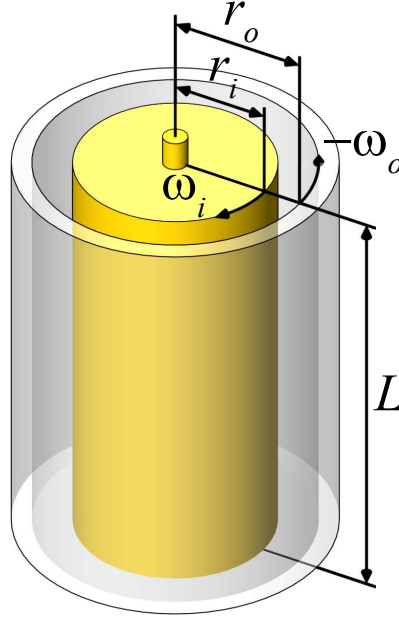


Figure 1: Schematic of the Taylor-Couette system. The system consists of two coaxial cylinders, which have an inner cylinder radius of  $r_i$  and an outer cylinder radius of  $r_o$ . Both cylinders are of length  $L$ . The inner cylinder rotates with an angular velocity  $\omega_i$  and the outer cylinder rotates with an angular velocity of  $\omega_o$ .

The geometry of TC is characterized by two nondimensional parameters, namely the radius ratio  $\eta = r_i/r_o$  and the aspect ratio  $\Gamma = L/d$ .

Instead of taking  $Re_i$  and  $Re_o$ , the driving in TC can alternatively be characterized by the Taylor  $Ta$  and the rotation rate, also called the Rossby  $Ro$  number. The Taylor number can be seen as the non-dimensional forcing (the differential rotation) of the system defined as  $Ta = \sigma(r_o - r_i)^2(r_o + r_i)^2(\omega_o - \omega_i)^2/(4\nu^2)$ , or

$$Ta = (r_a^6 d^2 / r_o^2 r_i^2 \nu^2) (\omega_o - \omega_i)^2. \quad (1.1)$$

Here  $\sigma = r_a^4 / r_g^4$  with  $r_a = (r_o + r_i)/2$  the arithmetic and  $r_g = \sqrt{r_o r_i}$  the geometric mean radii. The Rossby number is defined as:

$$Ro = \frac{|\omega_i - \omega_o| r_i}{2\omega_o d}, \quad (1.2)$$

and can be seen as a measure of the rotation of the system as a whole.  $Ro < 0$  corresponds to counterrotating cylinders, and  $Ro > 0$  to corotating cylinders.

TC is among the most investigated systems in fluid mechanics, mainly owing to its simplicity as an experimental model for shear flows. TC is in addition a closed system, so global balances which relate the angular velocity transport to the energy dissipation can be obtained. Specifically, in Eckhardt, Grossmann & Lohse (2007) (from now on referred to as EGL 2007), an exact relationship between the global parameters and the volume averaged energy dissipation rate was derived. This relationship has an analogous form to the one which can be obtained for Rayleigh-Bénard (RB) flow, i.e. a flow in which heat is transported from a hot bottom plate to a cold top plate.

TC and RB flow have been extensively used to explore new concepts in fluid me-

chanics. Instabilities (Pfister & Rehberg 1981; Pfister *et al.* 1988; Chandrasekhar 1981; Drazin & Reid 1981; Busse 1967), nonlinear dynamics and chaos (Lorenz 1963; Ahlers 1974; Behringer 1985; Dominguez-Lerma *et al.* 1986; Strogatz 1994), pattern formation (Andereck *et al.* 1986; Cross & Hohenberg 1993; Bodenschatz *et al.* 2000), and turbulence (Siggia 1994; Grossmann & Lohse 2000; Kadanoff 2001; Lathrop *et al.* 1992*b*; Ahlers *et al.* 2009; Lohse & Xia 2010) have been studied in both TC and RB and both numerically and experimentally. The main reasons behind the popularity of these systems are, in addition to the fact that they are closed systems, as mentioned previously, their simplicity due to the high amount of symmetries present. It is also worth noting that plane Couette flow is the limiting case of TC when the radius ratio  $\eta = 1$ .

Experimental investigations of TC have a long history, dating back to the seminal works by Wendt (1933) and Taylor (1936). Experimental work continued during the years (Smith & Townsend 1982; Andereck *et al.* 1986; Tong *et al.* 1990; Lathrop *et al.* 1992*b,a*; Lewis & Swinney 1999; van Gils *et al.* 2011*a,b*; Paoletti & Lathrop 2011; Huisman *et al.* 2012*b*) at low and high  $Ta$  numbers for different ratios of the rotation frequencies  $a = -\omega_o/\omega_i$ .  $a$  is positive for counter-rotation and negative for co-rotation.  $-a \equiv \mu$ , another measure used for the ratio of rotation frequencies. This work has been complemented by numerical simulations, not only in the regime of pure inner cylinder rotation (Fasel & Booz 1984; Coughlin & Marcus 1996; Dong 2007, 2008; Pirro & Quadrio 2008), but also for eigenvalue study (Gebhardt & Grossmann 1993), and counter-rotation at fixed  $a$  (Dong 2008). Recently (Brauckmann & Eckhardt 2013*a*; Ostilla *et al.* 2013*b*; Heise *et al.* 2013), simulations have also explored the effect of the outer cylinder rotation on the system.

The recent experiments (van Gils *et al.* 2011*a,b*; Paoletti & Lathrop 2011; Merbold *et al.* 2013) and simulations (Brauckmann & Eckhardt 2013*a*; Ostilla *et al.* 2013*b*) have shown that at fixed  $Ta$  an optimal angular momentum transport is obtained at *non-zero*  $a_{opt}$ , and that the location of this maximum  $a_{opt}$  varies with  $Ta$ . However, both experiments and simulations have been restricted to two radius ratios, namely  $\eta = 0.5$  and  $\eta = 0.714$ . The same radius ratios were also used for studies carried out on scaling laws of the torque and the “wind” of turbulence at highly turbulent Taylor numbers (Lewis & Swinney 1999; Paoletti & Lathrop 2011; van Gils *et al.* 2011*b*; Huisman *et al.* 2012*b*; Merbold *et al.* 2013). Up to now, it is not clear how the radius ratio affects the scaling laws of the system response or the recently found phenomena of optimal transport as a function of  $Ta$ .

Two suggestions were made to account for the radius ratio dependence of optimal transport. Van Gils *et al.* (2011*b*) wondered whether the optimal transport in general lies in or at least close to the Voronoi boundary (meaning a line of equal distance) of the Esser-Grossmann stability lines in the  $(Re_o, Re_i)$  phase space as it does for  $\eta = 0.714$ . However, this bisector value does not give the correct optimal transport for  $\eta = 0.5$  (Merbold *et al.* 2013; Brauckmann & Eckhardt 2013*b*). Therefore Brauckmann & Eckhardt (2013*a*) proposed a dynamic extension of the Esser-Grossmann instability theory. This model correctly gives the observed optimal transport (within experimental error bars) between  $\eta = 0.5$  and  $\eta = 0.714$  for three experimental data sets (Wendt 1933; Paoletti & Lathrop 2011; van Gils *et al.* 2011*b*) and one numerical data set (Brauckmann & Eckhardt 2013*b*), but it is not clear how it performs outside the  $\eta$ -range  $[0.5, 0.714]$ .

In this paper, we study the following questions: how does the radius ratio  $\eta$  affect the flow? How are the scaling laws of the angular momentum transport affected? What is the role of the geometric parameter called pseudo-Prandtl number  $\sigma$  introduced in EGL2007? Can the effect of the radius ratio be interpreted as a kind of non-Oberbeck-Boussinesq effect, analogous to this effect in Rayleigh-Bénard flow? Finally, are the predictions and

insights of van Gils *et al.* (2011b), Ostilla *et al.* (2013b) and Brauckmann & Eckhardt (2013b) on the optimal transport also valid for other values of  $\eta$ ?

In order to answer these questions, both direct numerical simulations (DNS) and experiments have been undertaken. Numerical simulations, with periodic axial boundary conditions, have been performed using the finite-difference code previously used in Ostilla *et al.* (2013b). In these simulations, three more values of  $\eta$  have been investigated: one in which the gap is larger ( $\eta = 0.5$ ), and two in which the gap is smaller ( $\eta = 0.833$  and  $0.909$ ). With the previous simulations from Ostilla *et al.* (2013b) at  $\eta = 0.714$ , a total of four radius ratios has been analyzed.

Figure 2 shows the  $(Ta, 1/Ro)$  parameter space explored in the simulations for the four selected values of the radius ratio  $\eta$ . A higher density of points has been used in places where the global response  $(Nu_\omega, Re_w)$  of the flow shows more variation with the control parameters  $Ta$  and  $1/Ro$ . A fixed aspect ratio of  $\Gamma = 2\pi$  has been taken for all simulations, and axially periodic boundary conditions have been used. These simulations have the same upper bounds of  $Ta$  (or  $Re_i$ ) as the ones of Ostilla *et al.* (2013b).

In addition to these simulations, experiments have been performed with the Twente Turbulent Taylor-Couette ( $T^3C$ ) facility, with which we achieve larger  $Ta$  numbers. Details of the setup are given in van Gils *et al.* (2011a). Once again, four values of  $\eta$  have been investigated, but, due to experimental constraints, we have been limited to investigate only smaller gap widths, i.e. values  $\eta \geq 0.714$ , namely  $\eta = 0.714, 0.769, 0.833$  and  $0.909$ . The experimentally explored parameter space are shown in Fig. 3.

The structure of the paper is as follows. In sections 2 and 3, we start by describing the numerical code and the experimental setup, respectively. In section 4, the global response of the system, quantified by the non-dimensionalized angular velocity current  $Nu_\omega$  is analyzed. To understand the global response, we analyze the local data which can be obtained from the DNS simulations in section 5. Angular velocity profiles in the bulk and in the boundary layers are analyzed and related to the global angular velocity optimal transport. We finish in section 6 with a discussion of the results and an outlook for further investigations.

## 2. Numerical method

In this section, the used numerical method is explained in detail. The rotating frame in which the Navier-Stokes equations are solved and the employed non-dimensionalizations are introduced in the first section. This is followed by detailing the spatial resolution checks which have been performed.

### 2.1. Code description

The employed code is a finite difference code, which solves the Navier-Stokes equations in cylindrical coordinates. A second-order spatial discretization is used, and the equations are advanced in time by a fractional time integration method. This code is based on the so-called Verzicco-code, whose numerical algorithms are detailed in Verzicco & Orlandi (1996). A combination of MPI and OpenMP directives are used to achieve large scale parallelization. This code has been extensively used for Rayleigh-Bénard flow; for recent simulations see Stevens *et al.* (2010, 2011). In the context of TC flow, Ostilla *et al.* (2013b) already validated the code for  $\eta = 0.714$ .

The flow was simulated in a rotating frame, which was chosen to rotate with  $\Omega = \omega_o e_z$ . This was done in order to simplify the boundary conditions. In that frame the outer cylinder is stationary for any value of  $a$ , while the inner cylinder has an azimuthal velocity of  $u_\theta(r = r_i) = r_i(\omega_i^\ell - \omega_o^\ell)$ , where the  $\ell$  superscript denotes variables in the lab frame,

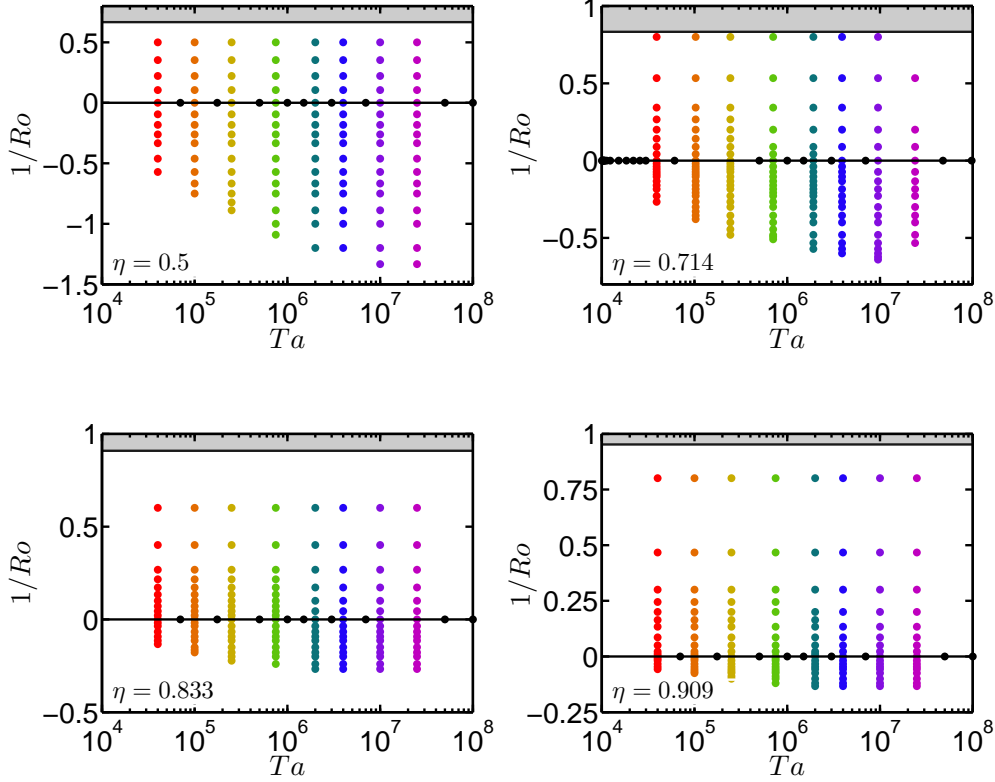


Figure 2: Control parameter phase space which was numerically explored in this paper in the  $(Ta, 1/Ro)$  representation. From top-left to bottom-right:  $\eta = 0.5$ ,  $0.714$ ,  $0.833$  and  $0.909$ .  $\Gamma = 2\pi$  was fixed, and axial periodicity was employed. The grey-shaded area signals boundary conditions for which the angular momentum  $L = r^2\omega$  of the outer cylinder ( $L_o$ ) is larger than the angular momentum of the inner cylinder ( $L_i$ ). This causes the flow to have an overall transport of angular momentum towards the inner cylinder. In this region, the Rayleigh stability criterium applies, which states that if  $dL/dr > 0$  the flow is linearly stable to axisymmetric perturbations.

while no superscript denotes variables in the rotating frame. We then choose the inner cylinder rotation rate in the rotating frame as the characteristic velocity of the system  $U \equiv |u_\theta(r_i)| = r_i|\omega_i - \omega_o|$  and the characteristic length scale  $d$  to non-dimensionalize the equations and boundary conditions.

It is worth noting that the characteristic velocity  $U$  can be written as

$$U = (\nu/d) \cdot [8\eta^2/(1+\eta)^3]^{1/2} \cdot Ta^{1/2}. \quad (2.1)$$

This means that up to a geometric factor depending on  $\eta$ , and which for our  $\eta$ 's is between  $0.6$  and  $1$ , the characteristic velocity Reynolds number  $Re \equiv Ud/\nu$  is simply  $Ta^{1/2}$ .

Using this non-dimensionalization, the inner cylinder velocity boundary condition simplifies to:  $\hat{u}_\theta(r = r_i) = \text{sgn}(\omega_i - \omega_o)$ . In this paper,  $\omega_i - \omega_o$  is always positive. Thus, in this rotating frame the flow geometry is simplified to a pure inner cylinder rotation with

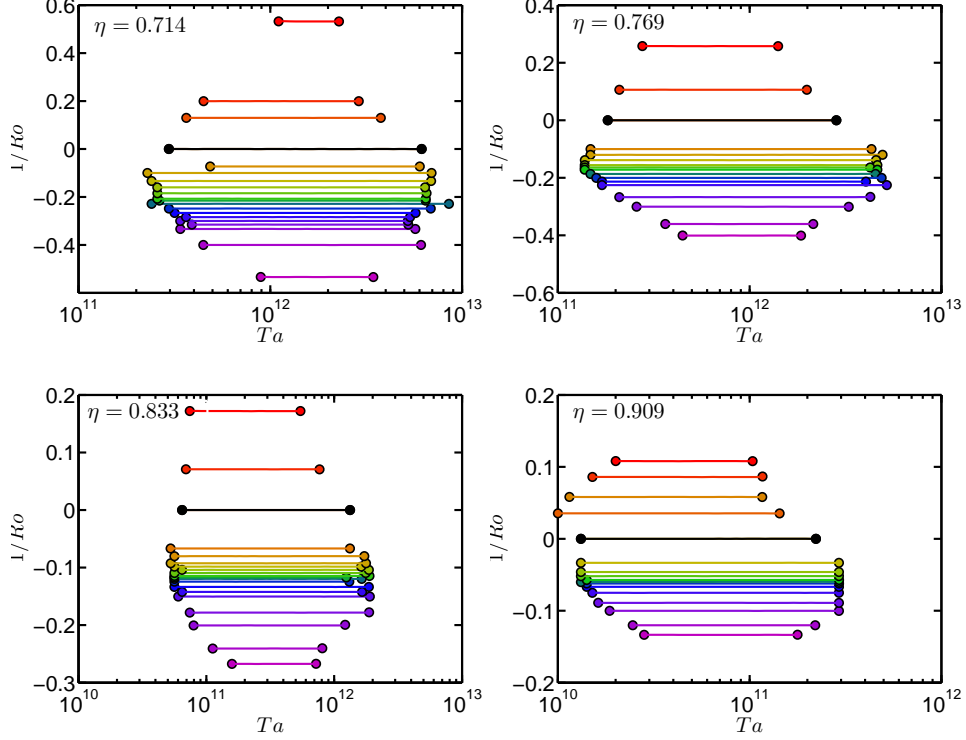


Figure 3: Control parameter phase space which was explored in experiments in the  $(Ta, Ro^{-1})$  representation for  $\eta = 0.716$  (top-left),  $\eta = 0.769$  (top-right),  $\eta = 0.833$  (bottom-left) and  $\eta = 0.909$  (bottom-right).

the boundary condition  $\hat{u}_\theta(r_i) = 1$ . The outer cylinder's effect on the flow is felt as a Coriolis force in this rotating frame of reference. The Navier-Stokes equations then read:

$$\frac{\partial \hat{\mathbf{u}}}{\partial t} + \hat{\mathbf{u}} \cdot \hat{\nabla} \hat{\mathbf{u}} = -\hat{\nabla} \hat{p} + \left( \frac{f(\eta)}{Ta} \right)^{1/2} \hat{\nabla}^2 \hat{\mathbf{u}} + Ro^{-1} \mathbf{e}_z \times \hat{\mathbf{u}}, \quad (2.2)$$

where  $Ro$  was defined previously in Eq. 1.2, and  $f(\eta)$  is

$$f(\eta) = \frac{(1 + \eta)^3}{8\eta^2}. \quad (2.3)$$

It is useful to continue the non-dimensionalization by defining the normalized radius  $\tilde{r} = (r - r_i)/d$  and the normalized height  $\tilde{z} = z/d$ . We define the time- and azimuthally-averaged velocity field as:

$$\hat{\mathbf{u}}(r, z) = \langle \hat{\mathbf{u}}(\theta, r, z, t) \rangle_{\theta, t}, \quad (2.4)$$

where  $\langle \phi(x_1, x_2, \dots, x_n) \rangle_{x_i}$  indicates averaging of the field  $\phi$  with respect to  $x_i$ .

To quantify the torque in the system, we first note that the angular velocity current

$$\mathcal{J}^\omega = r^3 (\langle u_r^\ell \omega^\ell \rangle_{\theta, z, t} - \nu \partial_r \langle \omega^\ell \rangle_{\theta, z, t}) \quad (2.5)$$

is conserved, i.e. independent on the radius  $r$  (EGL 2007).  $\mathcal{J}^\omega$  represents the current of

angular velocity from the inner cylinder to the outer cylinder (or vice versa). The first term is the convective contribution to the transport, while the second term is the diffusive contribution.

In the state with the lowest driving, and ignoring end plate effects, a laminar, time independent velocity field which is purely azimuthal,  $u_\theta^\ell(r) = Ar + B/r$ , with  $u_r = u_z = 0$ , is induced by the rotating cylinders. This laminar flow produces an angular velocity current  $J_0^\omega$ , which can be used to nondimensionalize the angular velocity current and a non-zero dissipation rate  $\epsilon_{u,0}$ .

$$Nu_\omega = \frac{J^\omega}{J_0^\omega}. \quad (2.6)$$

$Nu_\omega$  can be seen as an angular velocity ‘‘Nusselt’’ number.

When  $J^\omega$ , and therefore  $Nu_\omega$  are calculated numerically, the values will depend on the radial position, due to finite time averaging. We can define  $\Delta_J$  to quantify this radial dependence as:

$$\Delta_J = \frac{\max(J^\omega(r)) - \min(J^\omega(r))}{\langle J^\omega(r) \rangle_r} = \frac{\max(Nu_\omega(r)) - \min(Nu_\omega(r))}{\langle Nu_\omega(r) \rangle_r} \quad (2.7)$$

which analytically equals zero but will deviate when calculated numerically.

The convective dissipation per unit mass can be calculated either from its definition as a volume average of the local dissipation rate for an incompressible fluid,

$$\epsilon_u = \epsilon_u^\ell = \frac{\nu}{2} \langle (\partial_i^\ell u_j + \partial_j^\ell u_i)^2 \rangle_{V,t}, \quad (2.8)$$

or a global balance can also be used. The exact relationship (EGL 2007)

$$\epsilon_u^\ell - \epsilon_{u,0}^\ell = \frac{\nu^3}{d^4} \sigma^{-2} Ta (Nu_\omega - 1), \quad (2.9)$$

where  $\epsilon_{u,0}$  is the volume averaged dissipation rate in the purely azimuthal laminar flow, links the volume averaged dissipation to the global driving  $Ta$  and response  $Nu_\omega$ .

This link can be and has been used for code validation and for checking spatial resolution adequateness. The volume averaged dissipation can be calculated from both (2.8) and (2.9) and later checked for sufficient agreement. We define the quantity  $\Delta_\epsilon$  as the relative difference between the two ways of numerically calculating the dissipation, namely either via  $Nu_\omega$  with eq. 2.9 or directly from the velocity gradients, eq. 2.8:

$$\Delta_\epsilon = \frac{\nu^3 d^{-4} \sigma^{-2} Ta (Nu_\omega - 1) + \epsilon_{u,0}^\ell - \frac{\nu}{2} \langle (\partial_i^\ell u_j + \partial_j^\ell u_i)^2 \rangle_{V,t}}{\frac{\nu}{2} \langle (\partial_i^\ell u_j + \partial_j^\ell u_i)^2 \rangle_{V,t}}. \quad (2.10)$$

$\Delta_\epsilon$  is equal to 0 analytically, but will deviate when calculated numerically. The deviation of  $\Delta_J$  and  $\Delta_\epsilon$  from zero is an indication of the adequateness of the resolution.

We would like to emphasize that the requirement for  $\Delta_J < 0.01$  is much stricter than torque balance, which can simply be expressed as  $Nu_\omega(r_i) = Nu_\omega(r_o)$ . As analyzed in Ostilla *et al.* (2013b), a value of less than 1% for  $\Delta_J$  and about 1% for  $\Delta_\epsilon$  is linked to grid adequateness at the Taylor number simulated. To ensure convergence in time, the time-averages of the Nusselt number and the energy dissipation calculated locally (equation 2.8) were also checked to converge in time within 1%.

## 2.2. Resolution checks

Spatial resolution checks were performed in two ways. First, as mentioned previously, the values of  $\Delta_J$  and  $\Delta_\epsilon$  were checked. As an additional check, simulations at selected values of  $Ta$  were performed at a higher resolution. As the explored parameter space is large, these checks were performed only for the highest value of  $Ta$  simulated for the grid size. A lower driving of the flow for the same grid size is expected to have a smaller error due to spatial discretization, as spatial discretization errors increase with increased  $Re$ , and thus increased  $Ta$ .

Concerning the temporal resolution there are numerical and physical constraints; the former requires a time step small enough to keep the integration scheme stable and this is achieved by using an adaptive time step based on a Courant–Frederich–Lewy (*CFL*) criterium. The 3<sup>rd</sup>-order Runge–Kutta time-marching algorithm allows for a *CFL* of up to  $\sqrt{3}$ , but this can be reduced due to the implicit factorization of the viscous terms. For safety, the maximum *CFL* has been taken as 1.4. From the physical point of view, the time step size must also be small enough to properly describe the fast dynamics of the smallest flow scale which is the Kolmogorov scale. Although the time step size should be determined by the most restrictive among the two criteria above, our experience suggests that as long as the *CFL* number criterion is satisfied, which guarantees numerical stability, the results become insensitive to the time step size and all the flow scales are adequately described temporally. Direct confirmation of this statement can be found in Ostilla *et al.* (2013*b*).

The results for  $\eta = 0.5$ , 0.833, and 0.909 are presented in Table 1. Uniform discretization was used in azimuthal and axial directions. In the radial direction, points were clustered near the walls by using hyperbolic tangent-type clustering, or a clipped Chebyshev type clustering for higher values of  $Ta$ . A table including the results for the spatial resolution tests at  $\eta = 0.714$  can be found in Ostilla *et al.* (2013*b*).

## 3. Experimental setup

The Twente Turbulent Taylor-Couette (T<sup>3</sup>C) apparatus has been built to obtain high  $Ta$  numbers. It has been described in detail in van Gils *et al.* (2011*a*) and van Gils *et al.* (2012). The inner cylinder with outside radius  $r_i = 0.200$  m consists of three sections. The total height of those axially stacked sections is  $L = 0.927$  m. We measure the torque only on the middle section of the inner cylinder, which has a height of  $L_{\text{mid}} = 0.536$  m, to reduce end effects in our torque measurements. The transparent outer cylinder is made of acrylic and has an inside radius of  $r_o = 0.279$  m. We vary the radius ratio by reducing the diameter of the outer cylinder by adding a ‘filler’ that is fixed to the outer cylinder and sits between the inner and the outer cylinder, effectively reducing  $r_o$  while keeping  $r_i$  fixed. We have 3 fillers giving us 4 possible outer radii:  $r_o = 0.279$  m (without any filler), 0.26 m, 0.24 m, and 0.22 m, giving experimental access to  $\eta = 0.716$ , 0.769, 0.833, and 0.909, respectively. Note that by reducing the outer radius, we not only change  $\eta$ , but also change  $\Gamma = L/(r_o - r_i)$  from  $\Gamma(\eta = 0.716) = 11.68$  to  $\Gamma(\eta = 0.909) = 46.35$ .

For high  $Ta$  the heating up of the system becomes apparent and it has to be actively cooled in order to keep the temperature constant. We cool the working fluid (water) from the top and bottom end plates and maintain the temperature constant during any experiment. The setup has been constructed in such a way that we can rotate both cylinders independently while keeping the setup cooled.

As said before, we measure the torque on the middle inner cylinder. We do this by measuring the torque that is transferred from the axis to the cylinder by using a load-cell

---

| $\eta$ | $Ta$             | $N_\theta \times N_r \times N_z$ | $Nu_\omega$ | $100\Delta_J$ | $100\Delta_\epsilon$ | Case |
|--------|------------------|----------------------------------|-------------|---------------|----------------------|------|
| 0.5    | $2.5 \cdot 10^5$ | 100x100x100                      | 2.03372     | 0.30          | 1.11                 | R    |
| 0.5    | $2.5 \cdot 10^5$ | 150x150x150                      | 2.03648     | 0.76          | 0.89                 | E    |
| 0.5    | $7.5 \cdot 10^5$ | 150x150x150                      | 2.56183     | 0.47          | 0.92                 | R    |
| 0.5    | $7.5 \cdot 10^5$ | 256x256x256                      | 2.55673     | 0.74          | 0.31                 | E    |
| 0.5    | $1 \cdot 10^7$   | 300x300x300                      | 4.23128     | 0.33          | 1.07                 | R    |
| 0.5    | $1 \cdot 10^7$   | 400x400x400                      | 4.22574     | 0.97          | 1.06                 | E    |
| 0.5    | $2.5 \cdot 10^7$ | 350x350x350                      | 5.07899     | 0.85          | 1.12                 | R    |
| 0.5    | $2.5 \cdot 10^7$ | 512x512x512                      | 5.08193     | 0.87          | 1.98                 | E    |
| 0.5    | $5 \cdot 10^7$   | 400x400x400                      | 6.37233     | 0.23          | 3.68                 | R    |
| 0.5    | $1 \cdot 10^8$   | 768x512x1536                     | 7.48561     | 1.46          | 0.88                 | R    |
| 0.833  | $2.5 \cdot 10^5$ | 180x120x120                      | 2.72293     | 0.21          | 0.76                 | R    |
| 0.833  | $2.5 \cdot 10^5$ | 300x180x180                      | 2.72452     | 0.29          | 0.29                 | E    |
| 0.833  | $1 \cdot 10^7$   | 384x264x264                      | 7.07487     | 0.29          | 0.61                 | R    |
| 0.833  | $1 \cdot 10^7$   | 512x384x384                      | 7.17245     | 0.13          | 1.16                 | E    |
| 0.833  | $2.5 \cdot 10^7$ | 512x384x384                      | 8.62497     | 0.71          | 1.05                 | R    |
| 0.833  | $2.5 \cdot 10^7$ | 768x576x576                      | 8.51678     | 0.90          | 1.26                 | E    |
| 0.833  | $5 \cdot 10^7$   | 512x384x384                      | 9.68437     | 0.26          | 2.92                 | R    |
| 0.833  | $1 \cdot 10^8$   | 768x576x576                      | 11.4536     | 0.89          | 2.29                 | R    |
| 0.909  | $2.5 \cdot 10^5$ | 180x120x120                      | 2.31902     | 0.16          | 0.91                 | R    |
| 0.909  | $2.5 \cdot 10^5$ | 300x200x200                      | 2.30810     | 0.07          | 0.17                 | E    |
| 0.909  | $2 \cdot 10^6$   | 256x180x180                      | 3.76826     | 0.55          | 0.49                 | R    |
| 0.909  | $2 \cdot 10^6$   | 384x256x256                      | 3.77532     | 0.39          | 0.21                 | E    |
| 0.909  | $2.5 \cdot 10^7$ | 384x256x256                      | 7.83190     | 0.43          | 3.15                 | R    |
| 0.909  | $2.5 \cdot 10^7$ | 450x320x320                      | 7.86819     | 0.81          | 2.07                 | E    |
| 0.909  | $5 \cdot 10^7$   | 512x320x512                      | 9.07809     | 0.25          | 2.16                 | R    |
| 0.909  | $1 \cdot 10^8$   | 512x400x512                      | 10.9959     | 0.96          | 2.63                 | R    |

---

Table 1: Resolution tests for  $\Gamma = 2\pi$  and  $\eta = 0.5, 0.833$  and  $0.909$ . The first column displays the radius ratio, the second column displays the Taylor number, the third column displays the resolution employed, the fourth column the calculated  $Nu_\omega$ , the fifth column and sixth columns the relative discrepancies  $\Delta_J$  and  $\Delta_\epsilon$ , and the last column the 'case': (R)esolved and (E)rror reference.  $\Delta_\epsilon$  is positive, and exceeds the 1% threshold reported in Ostilla *et al.* (2013b) for some cases at the largest  $\eta$ , but even so resolution appears to be sufficient as variations of  $Nu_\omega$  are small.

---

that is inside the aforementioned cylinder. Torque measurements are performed using a fixed procedure: the inner cylinder is spun up to its maximum rotational frequency of 20 Hz and kept there for several minutes. Then the system is brought to rest. The cylinders are then brought to their initial rotational velocities (with the chosen  $1/Ro$ ), corresponding to a velocity for which the torque is accurate enough; generally of order 2–3 Hz. We then slowly increase both velocities over 3–6 hours to their final velocities while maintaining  $1/Ro$  fixed during the entire experiment. During this velocity ramp we continuously acquire the torque of this quasi-stationary state. The calibration of the system is done in a similar way; first we apply the maximum load on the system, going back to zero load, and then gradually adding weight while recording the torque. These procedures ensure that hysteresis effects are kept to a minimum, and that the system is always brought to the same state before measuring. More details about the setup can be found in van Gils *et al.* (2011a).

Local velocity measurements are done by laser Doppler anemometry (LDA). We mea-

sure the azimuthal velocity component by focusing two beams in the radial-azimuthal plane. We correct for curvature effects of the outer cylinder by using a ray-tracer, see Huisman *et al.* (2012a). The velocities are measured at midheight ( $z = L/2$ ) unless specified otherwise. For every measurement position we measured long enough such as to have a statistically stationary result.

#### 4. Global response: Torque

In this section, the global response of the TC system for the four simulated radius ratios is presented. This is done by measuring the scaling law(s) of the non-dimensional torque  $Nu_\omega$  as function(s) of  $Ta$ . The transition between different types of local scaling laws in different  $Ta$ -ranges is investigated, and related to previous simulations (Ostilla *et al.* 2013b) and experiments (van Gils *et al.* 2012).

##### 4.1. Pure inner cylinder rotation

The global response of the system is quantified by  $Nu_\omega$ . By definition, for purely azimuthal laminar flow,  $Nu_\omega = 1$ . Once the flow is driven stronger than a certain critical  $Ta$ , large azimuthal roll structures appear, which enhance angular transport through a large scale wind.

Figure 4 shows the response of the system for increasing  $Ta$  in case of pure inner cylinder rotation for four values of  $\eta$ . Experimental and numerical results are shown in the same panels, covering different ranges and thus complementary, but consistent with each other. Numerical results for  $\eta = 0.714$  from Ostilla *et al.* (2013a) have been added to both panels.

As has already been noticed in Ostilla *et al.* (2013b) for  $\eta = 0.714$ , a change in the local scaling law relating  $Ta$  to  $Nu_\omega$  occurs at around  $Ta \approx 3 \cdot 10^6$ . We can interpret these changes in the same way as Ostilla *et al.* (2013b) and relate the transition in the  $Ta$ - $Nu_\omega$  local scaling law to the break up of coherent structures.

It is also worth mentioning that the exponent in the local scaling laws in the regime before the transition depends on the radius ratio. This can be seen in the compensated plot, and explains the curve crossings that we see in the graphs.

For experiments (solid lines of figure 4), a different local scaling law can be seen. In this case the experiments are performed at much higher  $Ta$  than the simulations. The scaling  $Nu_\omega \sim Ta^{0.38}$  can be related to the so called “ultimate” regime, a regime where the boundary layers have become completely turbulent (Grossmann & Lohse 2011, 2012; Huisman *et al.* 2013). As indicated for the case at  $\eta = 0.714$  we expect that for increasing  $Ta$  also the simulations become turbulent enough to reach this scaling law (cf. Ostilla *et al.* (2013a)). In this regime, the local scaling law relating  $Ta$  and  $Nu_\omega$  has no dependence on  $\eta$  and thus is universal.

In both experiment and simulation with the largest  $Ta$ , the value of  $\eta$  corresponding to the smallest gap, i.e.  $\eta = 0.909$ , has the highest angular velocity transport ( $Nu_\omega$ ) at a given  $Ta$ . This can be phrased in terms of the pseudo-Prandtl-number  $\sigma$ , introduced in EGL2007. As a smaller gap means a smaller  $\sigma$ , we thus find a decrease of  $Nu_\omega$  with increasing  $\sigma$ , similarly as predicted Grossmann & Lohse (2001) and found Xia *et al.* (2002) for  $Nu(Pr)$  in RB convection for  $Pr > 1$ .

##### 4.2. Rossby number dependence

In this subsection, the effect of outer cylinder rotation on angular velocity transport will be studied. Previous experimental and numerical work at  $\eta = 0.714$  (Paoletti & Lathrop

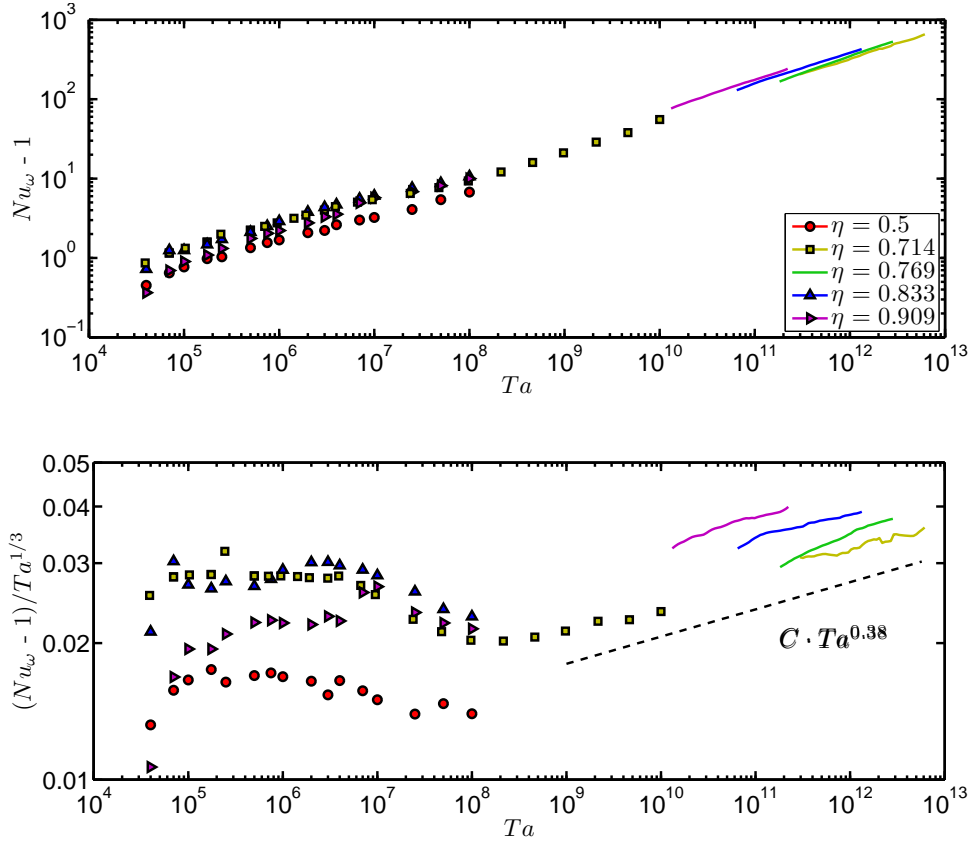


Figure 4: The global system response for pure inner cylinder rotation as function of the driving  $Ta$ : The top panel shows  $Nu_\omega - 1$  vs  $Ta$  for both simulations (points on the left of the graph) and experiments (lines on the right of the graph). Numerical data from Ostilla *et al.* (2013a) for  $\eta = 0.714$  have been added to these figures. The bottom panel shows the compensated Nusselt  $((Nu_\omega - 1)/Ta^{1/3})$  versus  $Ta$ .

2011; van Gils *et al.* 2011b; Ostilla *et al.* 2013b; Brauckmann & Eckhardt 2013a) revealed the existence of an optimum transport where, for a given  $Ta$ , the transport of momentum is highest at a Rossby number  $Ro_{opt}^{-1}$ , which depends on  $Ta$  and saturates around  $Ta \sim 10^{10}$ . In this subsection, this work will be extended to the other values of  $\eta$ .

Figure 5 shows the results of the numerical exploration of the  $Ro^{-1}$  parameter space between  $Ta = 4 \cdot 10^4$  and  $Ta = 2.5 \cdot 10^7$ . The shape of  $Nu_\omega = Nu_\omega(Ro^{-1})$  curves and the position of  $Ro_{opt}^{-1}$  depends very strongly on  $\eta$  in the  $Ta$  range studied in numerics. For the largest gap (i.e.,  $\eta = 0.5$ ), the optimum can be seen to be in the counter-rotating range (i.e.,  $Ro^{-1} < 0$ ) as long as  $Ta$  is high enough. On the other hand, for the smallest gap (i.e.,  $\eta = 0.909$ ), the optimum is at co-rotation (i.e.,  $Ro^{-1} > 0$ ) in the whole region studied. The other values of studied  $\eta$  reveal an intermediate behavior. Optimum transport is located for co-rotation at lower values of  $Ta$  and slowly moves towards counter-rotation. For all values of  $\eta$ , when the driving is increased,  $Ro_{opt}^{-1}$  tends to shift to more negative values.

The shift seen in the numerics may or may not continue with increasing  $Ta$ . The

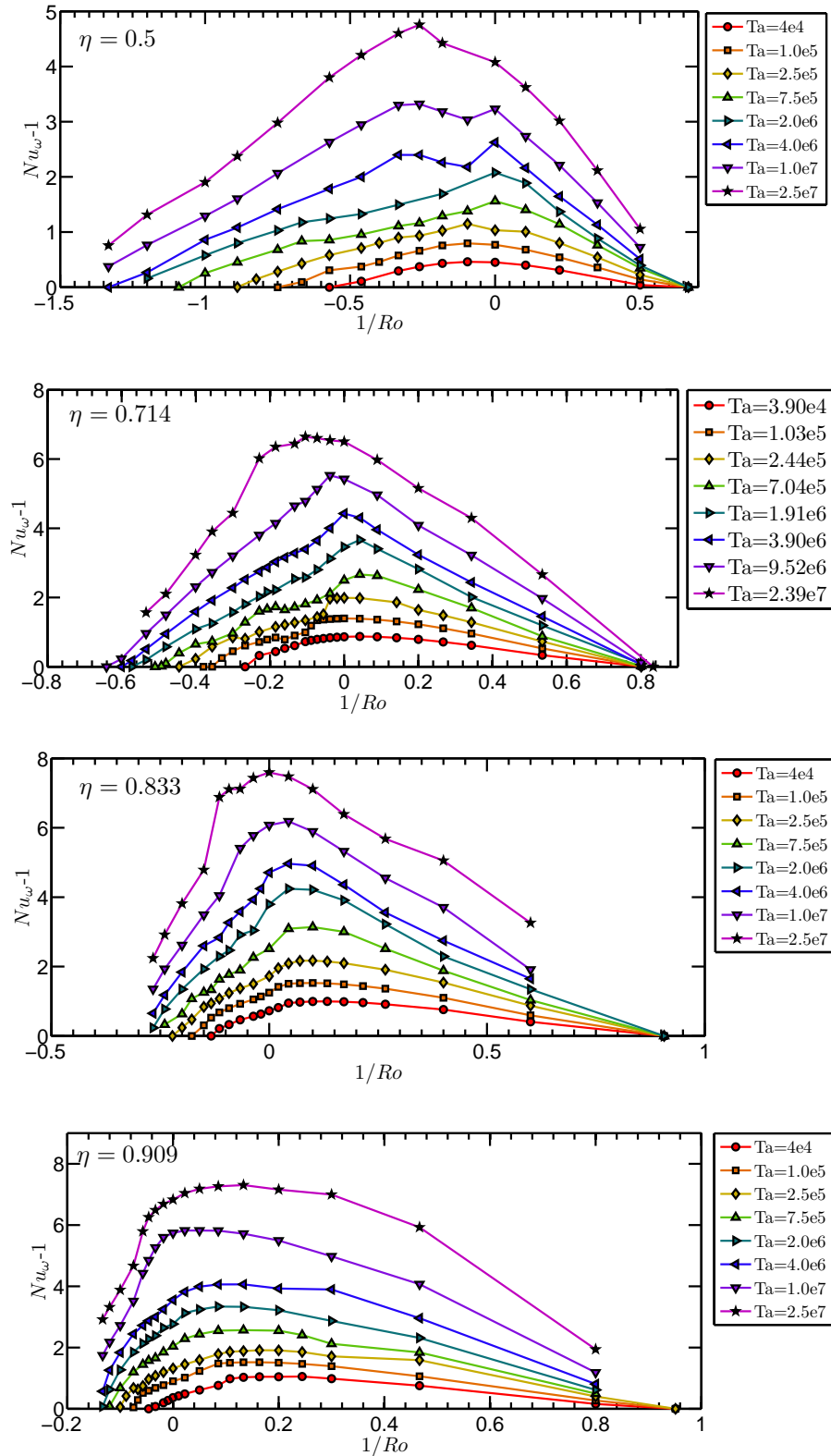


Figure 5:  $Nu_\omega - 1$  versus  $Ro^{-1}$  for the four values of  $\eta$  studied numerically,  $\eta = 0.5$  (top), 0.714, 0.833 and 0.909 (bottom). The shape of the curve and the position of the maximum depend very strongly on both  $Ta$  and  $\eta$ .

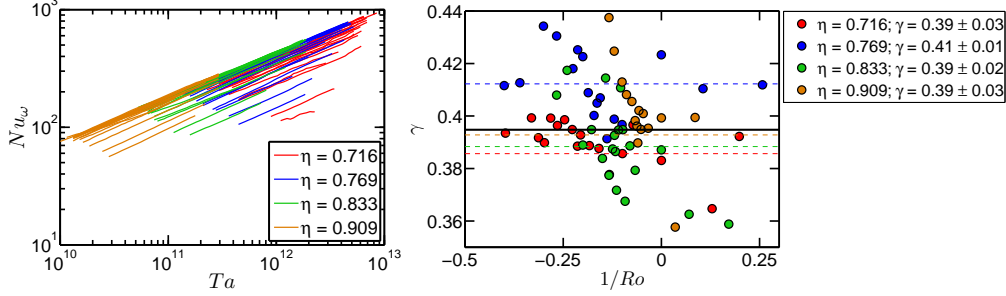


Figure 6: The left panel shows  $Nu_\omega$  versus  $Ta$  for all values of  $\eta$  and  $Ro^{-1}$  studied in experiments. The right panel shows the exponent  $\gamma$  of the scaling law  $Nu_\omega \propto Ta^\gamma$  for various  $Ro^{-1}$ , obtained by a least-square linear fit in log-log space. The average value of  $\gamma$  for each  $\eta$  is represented by the dashed lines, while the solid line represents the average value of  $\gamma = 0.39$  for all  $\eta$ , which will be used for compensating  $Nu_\omega$ .

experiments conducted explore a parameter space of  $10^{10} < Ta < 10^{13}$  and thus serve to explore the shift at higher driving. Figure 6 presents the obtained results. The left panel shows  $Nu_\omega$  versus  $Ta$  for all measurements. The right panel shows the exponent  $\gamma$ , obtained by fitting a least-square linear fit in the log-log plots. Across the  $\eta$  and  $Ro^{-1}$  range studied, the average exponent is  $\gamma \approx 0.39$ . This value is used in figure 7 to compensate  $Nu_\omega$ . The horizontality of all data points reflects the good scaling and the universality of this ultimate scaling behaviour  $Nu_\omega \propto Ta^{0.39}$ .

Figure 8 shows the shape of the  $Nu_\omega = Nu_\omega(Ro^{-1})$  or alternatively  $Nu_\omega = Nu_\omega(a)$  curve at the cut-off region highlighted in figure 7 from experiment. The increased driving changes the characteristics of the flow. This is reflected in the very different shapes of the  $Ro^{-1}$ -dependence of  $Nu_\omega$  when comparing figures 5 and 8, and in the shift of  $Ro_{opt}^{-1}$ .

To summarize these effects, figure 9 presents both the 85% peak width  $\Delta Ro_{max}^{-1}$  and the position of optimal transport  $Ro_{opt}^{-1}$  as a function of  $Ta$  and  $\eta$  obtained from numerics as well as the asymptotic value from experiments. The peak width  $\Delta Ro_{max}^{-1}$  is defined as:

$$\Delta Ro_{max}^{-1} = \frac{\int_{Ro_{-0.85}^{-1}}^{Ro_{0.85}^{-1}} Nu_\omega(Ro^{-1}) dRo^{-1}}{\max(Nu_\omega - 1)} \quad (4.1)$$

where  $Ro_{-0.85}^{-1}$  and  $Ro_{0.85}^{-1}$  are the values of  $Ro^{-1}$  for which  $Nu_\omega$  is 85% of the peak value.

The 85% peak width can be seen to vary with driving, reflecting what is seen in figure 5. The shape of the  $Ro^{-1}$ - $Nu_\omega$  curve is highly dependent of both  $\eta$  and  $Ta$ .  $Ro_{opt}^{-1}$  shows a very large variation across the  $Ta$  range studied in numerics. Therefore, one may ask the question: has the value of  $Ro_{opt}^{-1}$  already saturated in our experiments? Figure 7 shows the trend for  $Nu_\omega$  for increasing  $Ta$ . This trend does not seem to vary much for different values of  $Ro^{-1}$ . Therefore, we expect the value of  $Ro_{opt}^{-1}$  to have already reached saturation in our experiments.

We can compare these new experimental results to the speculations made in van Gils *et al.* (2012) and Brauckmann & Eckhardt (2013b) for the dependence of the saturated  $Ro_{opt}^{-1}$  on  $\eta$ . This is shown in figure 10. Both speculated dependencies are shown to deviate substantially from the experimental results obtained in the present work. Even if the

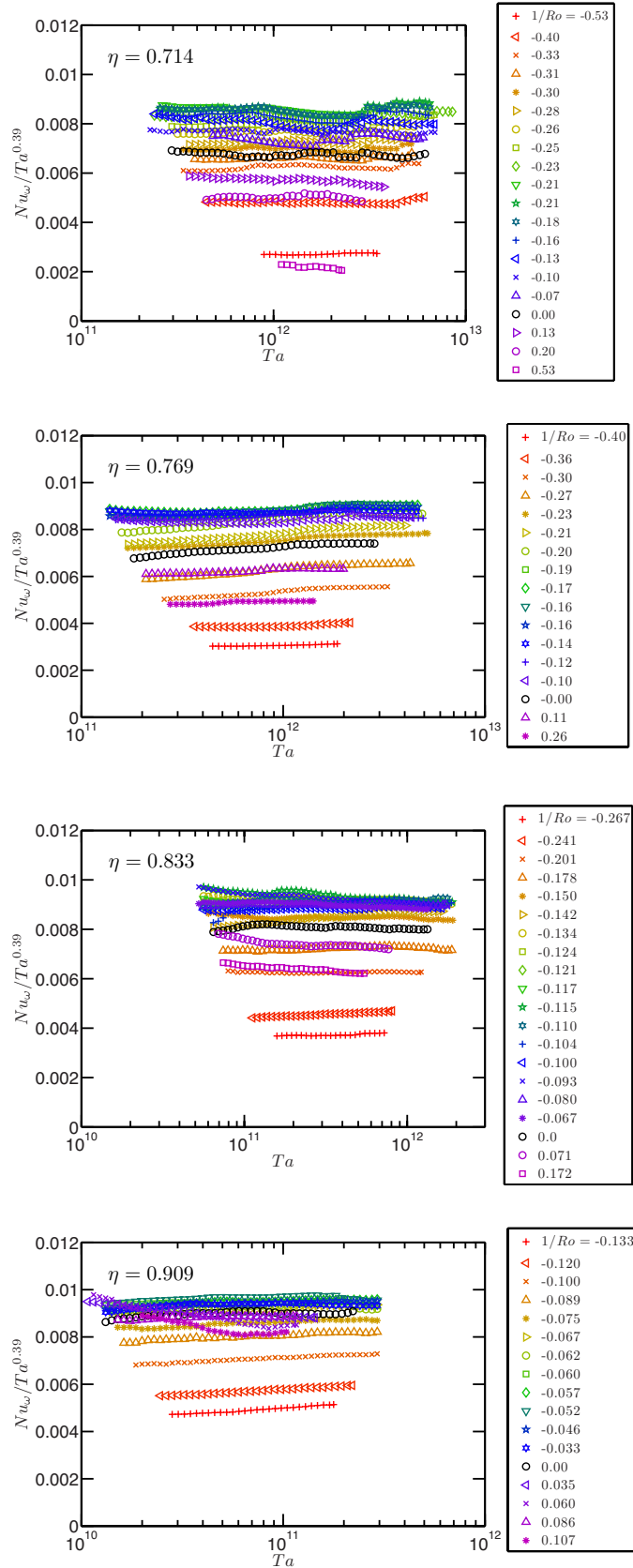


Figure 7: The four panels show  $Nu_\omega / Ta^{0.39}$  vs.  $Ta$  for all explored values of  $Ro^{-1}$  for the four studied values of  $\eta$  (top-to-bottom:  $\eta = 0.714$ , 0.769, 0.833, and 0.909, decreasing

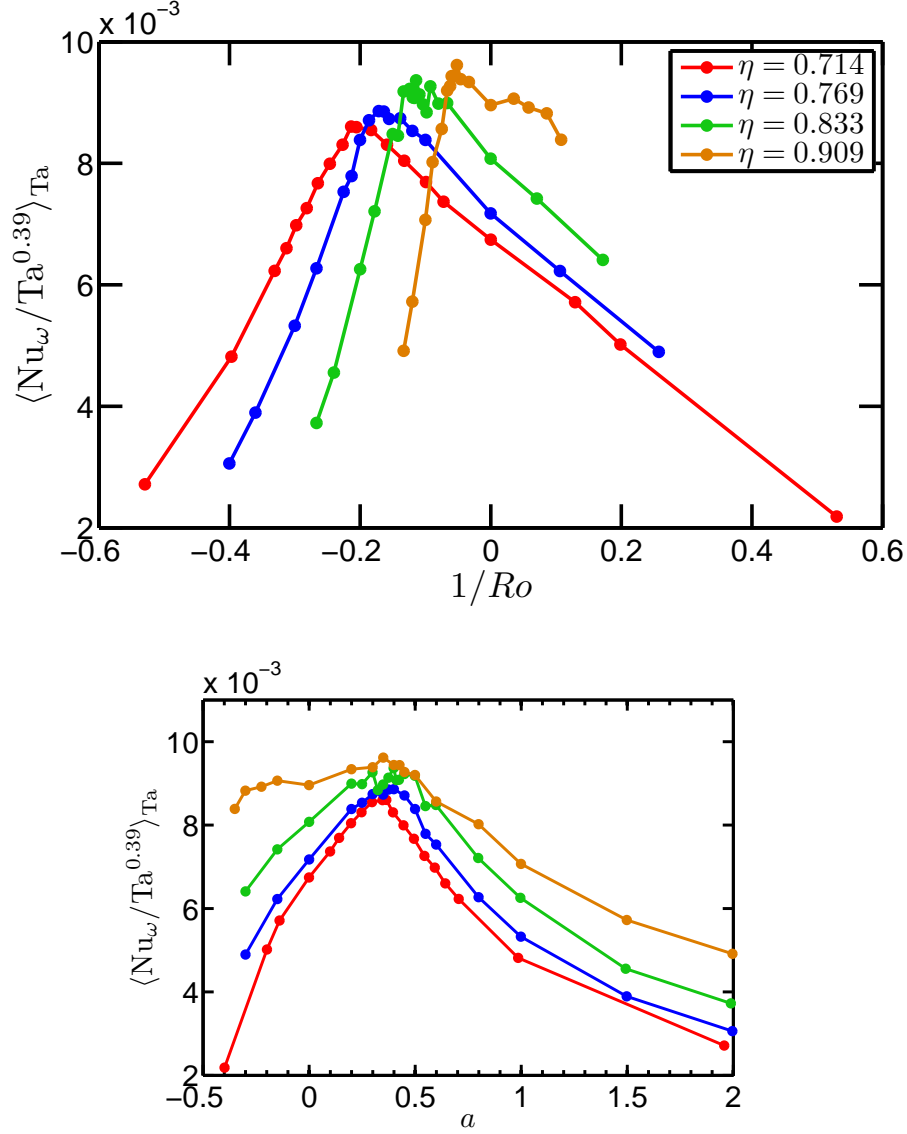


Figure 8: The panels show  $Nu_\omega / Ta^{0.39}$  versus either  $Ro^{-1}$  (top) or  $a$  (bottom) at the cut-off region highlighted in figure 7 for the values of  $\eta$  studied experimentally. There is a strong  $\eta$ -dependence of the curve  $Nu_\omega / Ta^{0.39}$  versus  $Ro^{-1}$ , even at the largest drivings studied in experiments. Optimal transport is located at  $Ro_{opt}^{-1} = -0.20$  for  $\eta = 0.714$ ,  $Ro_{opt}^{-1} = -0.15$  for  $\eta = 0.769$ ,  $Ro_{opt}^{-1} = -0.10$  for  $\eta = 0.833$  and  $Ro_{opt}^{-1} = -0.05$  for  $\eta = 0.909$ , corresponding to  $a \approx 0.33 - 0.35$  for all values of  $\eta$ . In the bottom panel, the maximum of the graph is less pronounced, i.e. it becomes more flat with increasing  $\eta$ . In the limit  $\eta \rightarrow 1$ ,  $a$  does not tend to a finite limit, while  $Ro^{-1}$  does. This result highlights the advantage of using  $Ro^{-1}$  instead of  $a$  as a control parameter.

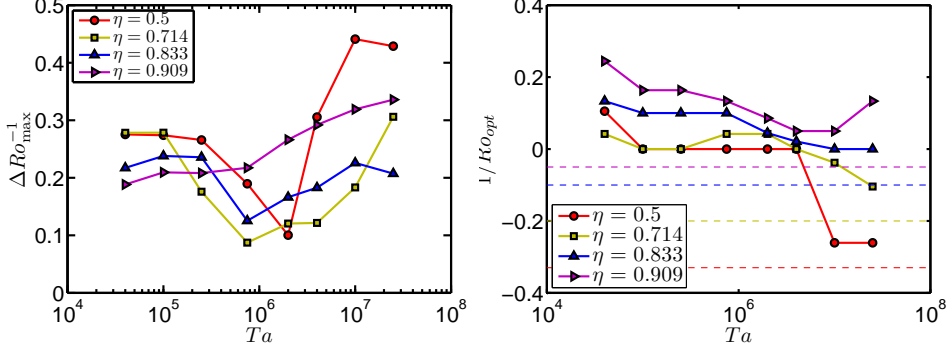


Figure 9: In the left panel, 85% peak width  $\Delta Ro_{max}^{-1}$  vs  $Ta$  for the four values of  $\eta$  analyzed in numerics. The peak width can be seen to vary with driving, and for smaller gaps is larger for larger values of  $Ta$ . In the right panel,  $Ro_{opt}^{-1}$  vs  $Ta$  for the same four values of  $\eta$ . The location of the optimal transport has a very strong dependence on the driving, especially for the largest values of  $\eta$ . As driving increases beyond the numerically studied range and overlaps with experiments,  $Ro_{opt}^{-1}$  should tend to the experimentally found values, represented as dashed lines in the figure. The asymptote for  $\eta = 0.5$  is obtained from Merbold *et al.* (2013). The trend appears to be less clear for  $\eta = 0.909$ , but this might be understandable from the peak width at the highest driving  $Ta$ .

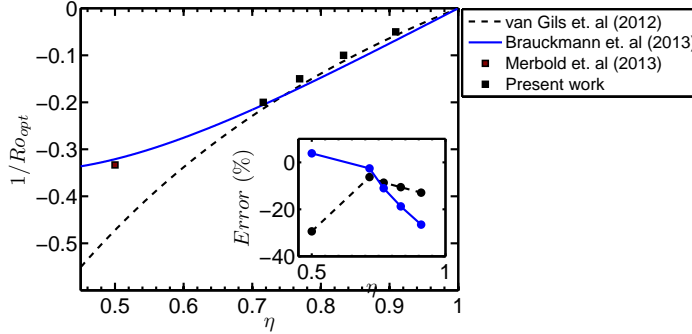


Figure 10: Experimental results for  $Ro_{opt}^{-1}$  are compared to the speculations of van Gils *et al.* (2012) and Brauckmann & Eckhardt (2013b). The inset shows the relative error of both speculations for the location of optimal transport. The new experimental results deviate up to 10% from the van Gils *et al.* (2012) and up to 30% from the Brauckmann & Eckhardt (2013b) speculations, while the results from Merbold *et al.* (2013) are within error bars of Brauckmann & Eckhardt (2013b) speculations and deviate up to 30% from the van Gils *et al.* (2012) speculations.

speculation from van Gils *et al.* (2012) appears to be better for this  $\eta$ -range, for previous experimental data at  $\eta = 0.5$ , it is in clear conflict with the experimentally measured value for optimal transport by Merbold *et al.* (2013).

This section has shown that the radius ratio has a very strong effect on the global response and especially on optimal transport. Significantly increased transport for co-rotation has been found at the lowest drivings based on the DNS results. This finding was already reported in Ostilla *et al.* (2013b) for  $\eta = 0.714$ , but the transport increase

was marginal. For  $\eta = 0.833$  and especially for  $\eta = 0.909$  the transport can be increased up to three times. The shift of  $Ro_{opt}^{-1}$  has also been seen to be much bigger and to happen in a much slower way for smaller gaps. The reason for this will be studied in Section 5, using the local data obtained from experiments and numerics.

## 5. Local results

In this section, the local angular velocity profiles will be analyzed. Angular velocity is the transported quantity in TC flow and shows the interplay between the bulk, where the transport is convection dominated, and the boundary-layers, where the transport is diffusion dominated. Numerical profiles and experimental profiles obtained from LDA will be shown. The angular velocity gradient in the bulk will be analyzed and connected to the optimal transport. In addition, the boundary layers will be analyzed and compared to the results from the analytical formula from EGL 2007 for the BL thickness ratio in the non-ultimate regime.

### 5.1. Angular velocity profiles

Angular velocity  $\omega$  profiles obtained from numerics are shown in figure 11. Results are presented for four values of  $\eta$  and selected values of  $Ro^{-1}$  at  $Ta = 2.5 \cdot 10^7$  (and  $Ta = 2.39 \cdot 10^7$  for  $\eta = 0.714$ ). Experimental data obtained by using LDA are shown in figure 12 for three values of  $\eta$ : from top-left to bottom,  $\eta = 0.714$  for  $Re_i - Re_o = 10^6$ ,  $\eta = 0.833$  for  $Ta = 5 \cdot 10^{11}$ , and  $\eta = 0.909$  for  $Ta = 1.1 \cdot 10^{11}$ .

The different radius ratios affect the angular velocity profiles on both boundary layers, as the two boundary layers are more asymmetric for the wide gaps; and they affect the bulk, as the bulk angular velocity is smaller for wide gaps. These effects will be analyzed in the next sections.

### 5.2. Angular velocity profiles in the bulk

We now analyze the properties of the angular velocity profiles in the bulk. We find that the slope of the profiles in the bulk is controlled mainly by  $Ro^{-1}$  and less so by  $Ta$ . This can be understood as follows: The Taylor number  $Ta$  acts through the viscous term, dominant in the boundary layers, while  $Ro^{-1}$  acts through the Coriolis force, present in the whole domain. These results extend the finding from Ostilla *et al.* (2013b) to other values of  $\eta$ .

To further quantify the effect of  $Ro^{-1}$  on the bulk profiles, we calculate the gradient of  $\langle \bar{\omega} \rangle_z$ . This is done by numerically fitting a tangent line to the profile at the inflection point using the two neighboring points on both sides; such fit is shown in the left panel of figure 13.

Figure 14 shows four panels, each containing the angular velocity gradient in the bulk from the numerical simulations and experiments for a given value of  $\eta$ . We first notice that the angular velocity gradients from experiment and numerics are in excellent agreement. Next the connection between a flat angular velocity profile and optimal transport can now be seen for other values of  $\eta$  and not just for  $\eta = 0.714$  as reported previously (van Gils *et al.* 2011b). Once  $Ro^{-1} < Ro_{opt}^{-1}$ , the large scale balance analyzed in Ostilla *et al.* (2013b) breaks down, and a “neutral” surface which reduces the transport appears in the flow.

In simulations, because of resolution requirements, we are unable of driving the flow strongly enough to see a totally flat bulk profile. In Ostilla *et al.* (2013b), a linear extrapolation of the bulk angular velocity gradient was done to give an estimate for the case when this profile would become horizontal, i.e.,  $d\langle \bar{\omega} \rangle_z / d\tilde{r} = 0$ , and thus give an estimate

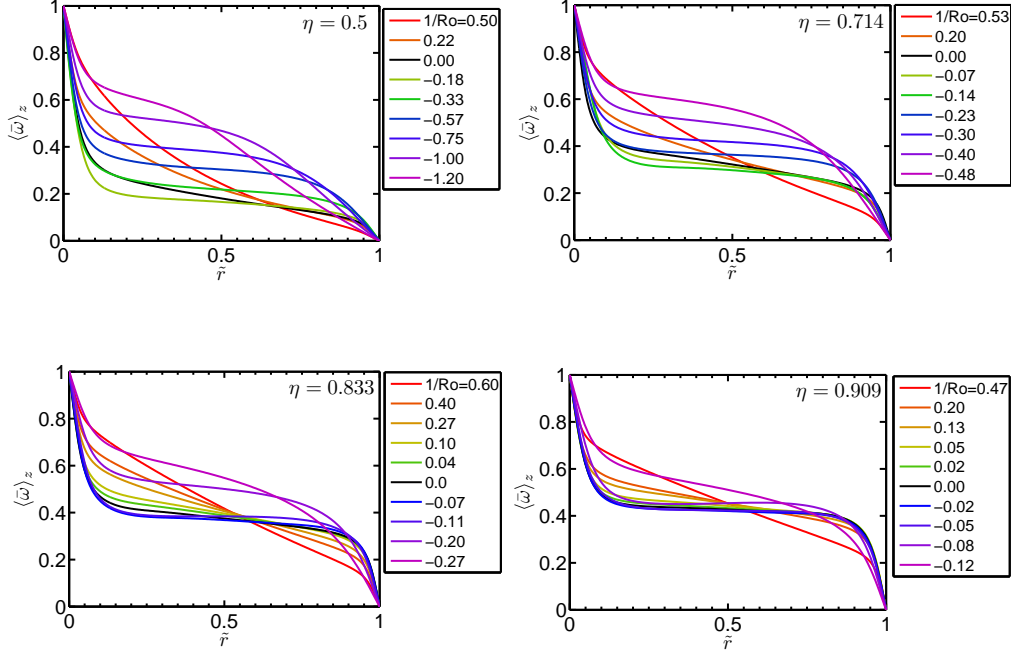


Figure 11: Azimuthally, axially and temporally averaged angular velocity  $\langle \bar{\omega} \rangle_z$  versus radius  $\tilde{r}$  for:  $\eta = 0.5$ ,  $\eta = 0.714$ ,  $\eta = 0.833$ , and  $\eta = 0.909$ . Data is for  $Ta = 2.5 \cdot 10^7$  ( $Ta = 2.39 \cdot 10^7$  for  $\eta = 0.714$ ) and selected values of  $Ro^{-1}$ . For smaller  $\eta$ , the  $\omega$ -bulk profiles differ more from a straight line, and have, on average, a smaller value.

of  $Ro_{opt}^{-1}$ . For  $\eta = 0.714$  this estimate agreed with the numerical result within error bars. Here, we extend this analysis for the other values of  $\eta$  and, as we shall see, successfully.

As in Ostilla *et al.* (2013b), an almost linear relationship between  $Ro^{-1}$  and  $d\langle \bar{\omega} \rangle_z / d\tilde{r}$  can be seen. This linear relationship is extrapolated and plotted in each panel. This extrapolation gives an estimate for  $Ro_{opt}^{-1}(Ta \rightarrow \infty)$ , which we can compare to the experimentally determined  $Ro_{opt}^{-1}(Ta \rightarrow \infty)$ . For  $\eta = 0.833$ ,  $Ro_{opt}^{-1}(Ta \rightarrow \infty) \approx -0.12$  corresponding to  $a \approx 0.38$  is obtained, and for  $\eta = 0.909$ ,  $Ro_{opt}^{-1}(Ta \rightarrow \infty) \approx -0.05$ , corresponding to  $a \approx 0.31$  is obtained. These values are (within error bars) also obtained for  $Ro_{opt}^{-1}$  at the large  $Ta$  investigated in experiments, namely  $Ro_{opt}^{-1} = -0.10$  and  $-0.05$ , respectively.

For  $\eta = 0.5$ ,  $Ro_{opt}^{-1}(Ta \rightarrow \infty) \approx -0.33$  is obtained, corresponding to  $a \approx 0.2$ . This value is consistent with the numerical results in Brauckmann & Eckhardt (2013b), which report  $a_{opt} \approx 0.2$ . However, care must be taken, as fitting straight lines to the  $\omega$ -profiles gives higher residuals for  $\eta = 0.5$  as the profiles deviate from straight lines (cf. top-left panel of figure 11). A fit to the “quarter-Couette” profile derived from upper bound theory (Busse 1967) is much more appropriate for  $\eta = 0.5$  at the strongest drivings achieved in experiments (Merbold *et al.* 2013). This is because the flow feels much more the effect of the curvature at the small  $\eta$ . On the other end of the scale, the linear relationship works best for smallest gaps, i.e.  $\eta = 0.909$  (cf. the bottom right panel of figure 11) where curvature plays a small effect.

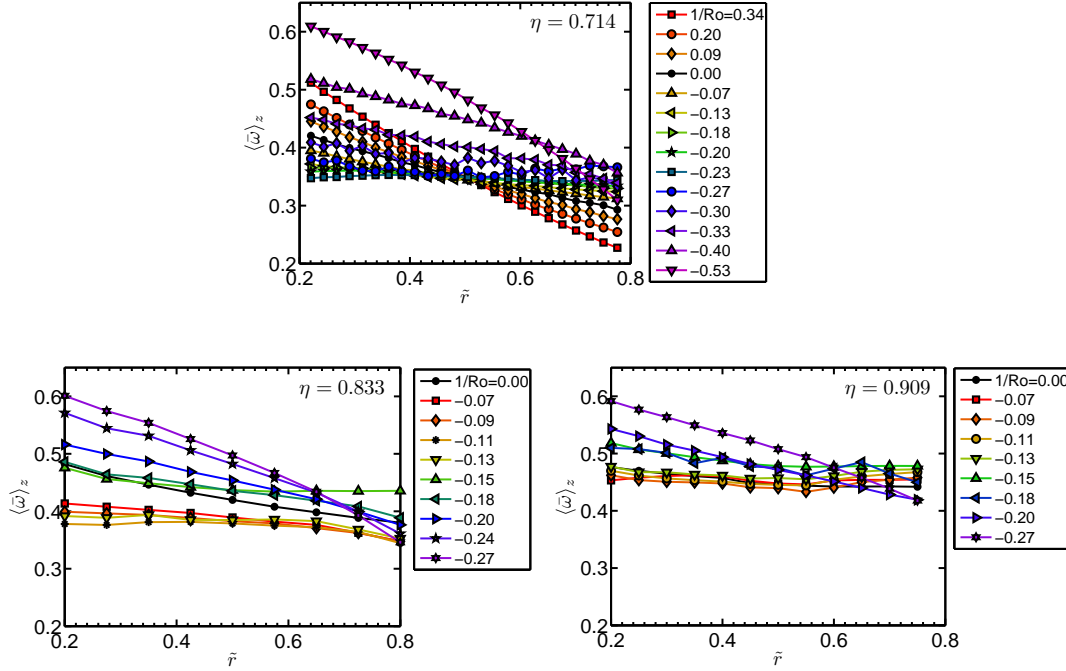


Figure 12: Angular velocity profiles obtained by LDA for  $\eta = 0.714$  at either  $Re_i - Re_o = 10^6$  (top-left),  $\eta = 0.833$  or at  $Ta = 5 \cdot 10^{11}$  (top-right) and  $\eta = 0.909$  at  $Ta = 1.1 \cdot 10^{11}$  (bottom), to explore different dependencies in parameter space. Data is taken at a fixed axial height, but as the Taylor number  $Ta$  is much larger than in the numerics, the axial dependence is much weaker.

### 5.3. Angular velocity profiles in the boundary layers in the classical turbulent regime

As the driving is increased, the transport is enhanced. To accommodate for this, the boundary layers (BLs) become thinner and therefore the  $\omega$ -slopes ( $\partial_r \omega$ ) become steeper. Due to the geometry of the TC system an intrinsic asymmetry in the BL layer widths is present. More precisely, the exact relationship  $\partial_r \langle \omega \rangle_o = \eta^3 \partial_r \langle \omega \rangle_i$  holds for the slopes of the boundary layers, due to the  $r$  independence of  $J^\omega$ , cf. EGL 2007 and eq.(2.5).

An analysis of the boundary layers was not possible in the present experiments because the present LDA measurements have insufficient spatial resolution to resolve the flow in the near-wall region. Therefore, only DNS results will be analyzed here. In simulations the driving is not as large as in experiments, and as a consequence the shear in the BLs is expected to not be large enough to cause a shear-instability. This means that the BLs are expected to be of Prandtl-Blasius (i.e. laminar) type, even if the bulk is turbulent. On the other hand, in the experiments both boundary layers and bulk are turbulent, i.e. the system is in the “ultimate regime”.

Using the DNS data, we can compare the ratio of the numerically obtained boundary layer widths with the analytical formula for this ratio obtained by EGL 2007 for laminar boundary layers, namely:

$$\frac{\lambda_\omega^o}{\lambda_\omega^i} = \eta^{-3} \frac{|\omega_o - \omega_{bulk}|}{|\omega_i - \omega_{bulk}|}, \quad (5.1)$$

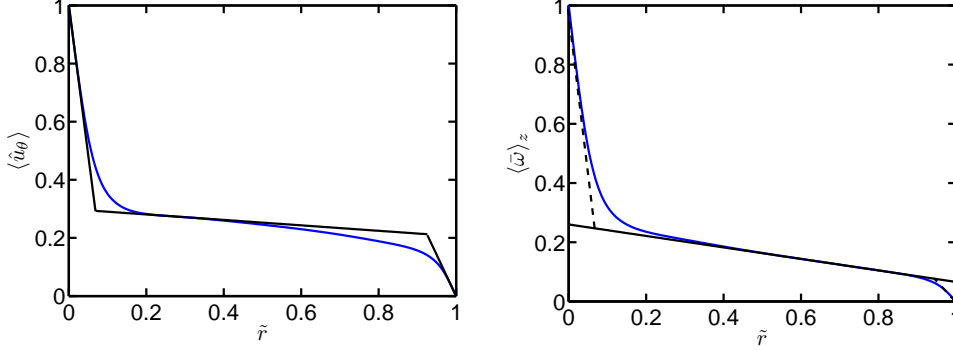


Figure 13: An example of the two fitting procedures for the bulk angular velocity gradient and for boundary layer thicknesses is shown here. Both panels show the  $\theta, z$ , and  $t$  averaged azimuthal velocity and angular velocity for  $\eta = 0.5$ ,  $Ta = 1 \cdot 10^7$ , and pure inner cylinder rotation. In the left panel a line is fitted to the bulk of the angular velocity to obtain the bulk gradient. The right panel shows the three-lines-fit to the whole profile to obtain the width of its boundary layers, used in Section 5.3. Both bulk fits are done at the inflection point, but for different variables ( $\bar{\omega}$  or  $\bar{u}_\theta$ ), which gives slightly different slopes (and intersection points).

where the value of  $\omega_{bulk}$  is some appropriate value in between for which the angular velocity at the inflection point of the profile might be chosen, i.e., the point at which the linear bulk profile fit was done to obtain  $\lambda_\omega^o$  and  $\lambda_\omega^i$ . The value  $\omega_{bulk}$  is taken from the numerics, and may bias the estimate.

To calculate the boundary layer thicknesses, the profile of the mean azimuthal velocity  $\langle \bar{u}_\theta \rangle_z$  is approximated by three straight lines, one for each boundary layer and one for the bulk. For the boundary layers the slope of the fit is calculated by fitting (by least-mean-squares) a line through the first two computational grid points. For the bulk, first the line is forced to pass through the grid point which is numerically closest to the inflection point of the profile. Then its slope is taken from a least mean square fit using two grid points on both sides of this inflection point. The respective boundary layer line will cross with this bulk line at a point which then defines the thickness of that boundary layer.

The results obtained for  $\lambda_\omega^o/\lambda_\omega^i$  both from equation 5.1 and directly from the simulations is shown in figure 14. Results are presented for the four values of  $\eta$  and only for the highest value of  $Ta$  achieved in the simulations. The boundary layer asymmetry for counter-rotating cylinders (i.e.,  $Ro^{-1} < 0$ ) grows with larger gaps. This is to be expected, as the  $\eta^{-3}$  term is much larger ( $\approx 8$ ) for the largest gap as compared to the smallest gap ( $\approx 1.3$ ). This is consistent with the  $\eta$  and thus  $\sigma$  restriction in EGL 2007 to a range of smaller gap widths.

As noticed already in Ostilla *et al.* (2013b) we find that the fit is not satisfactory for co-rotation (i.e.,  $Ro^{-1} > 0$ ) at the lowest values of  $\eta$ , but is satisfactory for counter-rotation (ie.  $Ro^{-1} < 0$ ). This can be explained from the fact that in EGL 2007, equation (5.1) is obtained by approximating the profile by three straight lines, two for the BLs and a constant  $\omega$  line for the bulk. This does not hold very well for co-rotating cylinders, where the bulk has a steep gradient (see figure 15). The steepness of the gradient in the bulk is larger for smaller values of  $\eta$  as seen in Section 5.2. This is why the formula fails for  $\eta = 0.5$ .

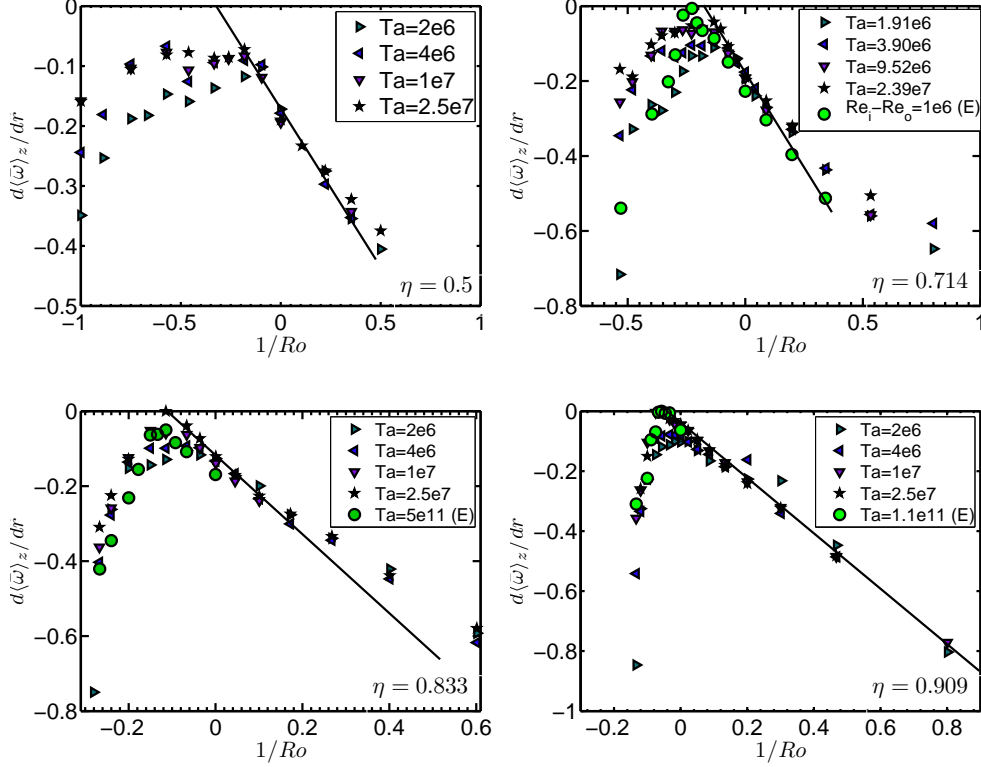


Figure 14: Bulk angular velocity gradient  $d\langle\bar{\omega}\rangle_z/d\tilde{r}$  against  $Ro^{-1}$  for the four values of  $\eta$  explored in simulations,  $\eta = 0.5$  (top left),  $\eta = 0.714$ , (top right),  $\eta = 0.833$ , (bottom left), and  $\eta = 0.909$  (bottom right). Data from experiments obtained by LDA is also plotted for the three values of  $\eta$  for which it was experimentally measured (green circles). For all values of  $\eta$  except  $\eta = 0.5$ , for co-rotation and slight counter-rotation there is once again an almost linear relationship between  $Ro^{-1}$  and  $d\langle\bar{\omega}\rangle_z/d\tilde{r}$ . A black straight line is added to extrapolate this relationship in order to estimate  $Ro_{opt}^{-1}$ . A plateau, in which the radial gradient of  $\langle\bar{\omega}\rangle_z$  is small can be seen around optimal transport, indicating a large convective transport of angular velocity.

For co-rotation the boundary layers are approximately of the same size, and the ratio  $\lambda_\omega^o/\lambda_\omega^i$  is very close to 1. If one inverts equation (5.1) by approximating this ratio by 1, an estimate of what the angular velocity will be in the bulk due to the boundary layer slope asymmetry is obtained:

$$\omega_{bulk} = \frac{\eta^3}{1 + \eta^3}, \quad (5.2)$$

corresponding to:

$$\omega_{bulk}^\ell = \frac{-\omega_o^\ell + \eta^3 \omega_i^\ell}{1 + \eta^3}, \quad (5.3)$$

in the lab frame. This expression gives an estimate for  $\omega_{bulk}$  when the profile is flattest, and has been represented graphically in figure 11. Indeed, one can take this estimate (for

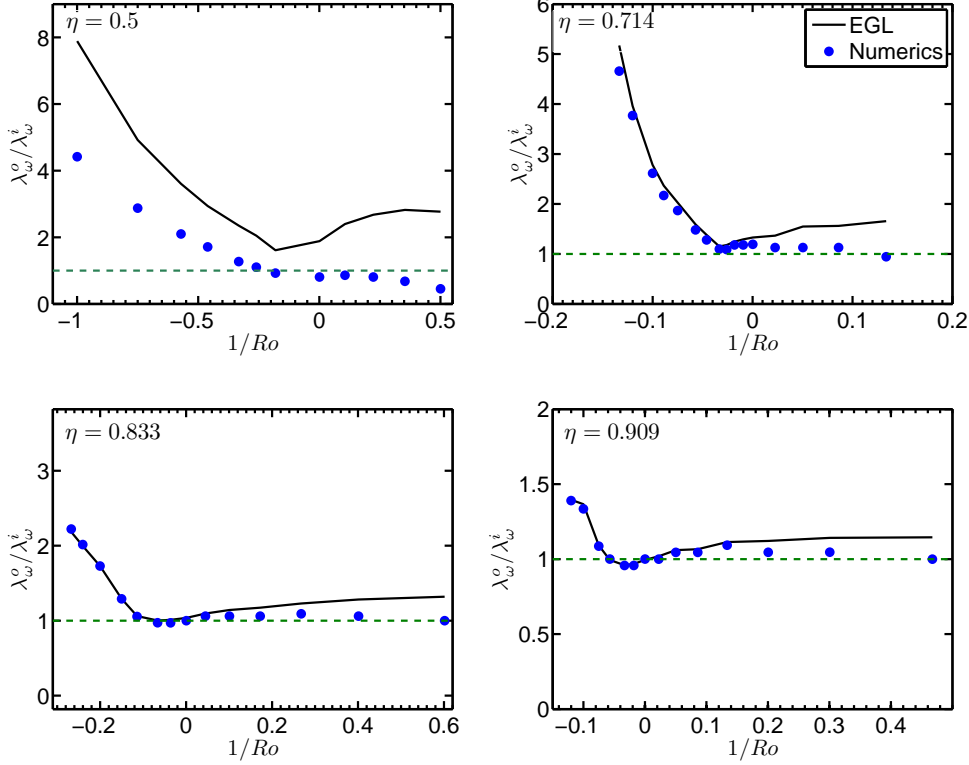


Figure 15:  $\lambda_\omega^o/\lambda_\omega^i$  from simulations (dots) and from equation (5.1) (solid lines) versus  $Ro^{-1}$  for the four values of  $\eta$  studied numerically,  $\eta = 0.5$  (top-left),  $0.714$  (top-right),  $0.833$  (bottom-left) and  $0.909$  (bottom-right) at  $Ta = 2.5 \cdot 10^7$ . The numerical results and the estimate from equation (5.1) match very well for larger values of  $\eta$  and especially for counter-rotating cylinders ( $1/Ro < 0$ ). The asymmetry between the boundary layers can be seen to be larger for smaller values of  $\eta$ , which is expected as equation (5.1) contains the explicit factor  $\eta^{-3}$ .

example 0.27 for  $\eta = 0.714$ ) and compare it with figures 11 and 12. We note that the value of  $\omega$  in the bulk for the flattest profile in the numerics (at  $Ro^{-1} \approx Ro_{opt}^{-1}(Ta)$ ) lies around  $\omega_{bulk}$ . We can also notice that the profiles for  $Ro^{-1} > Ro_{opt}^{-1}$  approximately cross each other at the same point, and this point has a value of  $\omega \approx \omega_{bulk}$ . This effect can only be seen in the numerics, as these approximations break down once the boundary layers become turbulent. The cross points of the curves are taken as an estimate for  $\omega_{bulk}$ , and this is represented against eq. 5.2 in figure 16.

To understand why the boundary layers are of approximately the same thickness despite the different initial slopes at the cylinders one has to go back to equation (2.5). The angular velocity current has a diffusive part and a convective part. Per definition in the boundary layer the diffusion dominates and in the bulk the convection does. Thus the boundary layer ceases when convection becomes significant. But convection is controlled by the wind. Thus in essence the boundary layer size is controlled by the wind and not immediately by the initial slope at the wall. Due to continuity, if the rolls penetrate the whole domain the wind may be expected to be the same close to the inner and close to

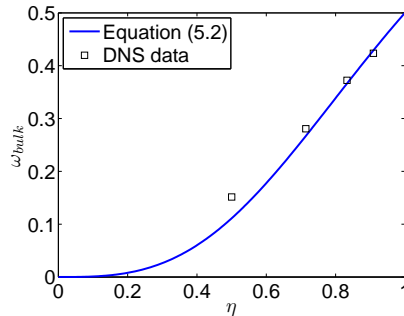


Figure 16:  $\omega_{bulk}$  as a function of  $\eta$ , taken from both eq. 5.2 and from the crosspoints of the  $\omega$ -profiles in figure 11. The trend is the same in both data sets. A smaller value of  $\eta$  decreases the value of the bulk angular velocity.

the outer cylinder. This suggests that the flow organizes itself in a way that the boundary layer extensions (or widths) might be similar, even if the initial slopes at the walls are different.

What happens for counter-rotation, or more precisely when  $Ro^{-1} < Ro_{opt}^{-1}$ ? For  $Ro^{-1}$  below the optimum  $Ro_{opt}^{-1}$  a so-called neutral surface will be present in the flow, which separates the Rayleigh-stable and -unstable areas. The wind drastically changes in the Rayleigh-stable areas (Ostilla *et al.* 2013b), leading to very different wind velocities close to the outer and inner cylinder, respectively. The wind at the outer cylinder will be weaker, as the rolls cannot fully penetrate the Rayleigh-stable domain. This means that the outer cylinder boundary layer will extend deeper into the flow, in accordance to what is seen in figure 15.

## 6. Summary and conclusions

Experiments and direct numerical simulations (DNS) were analysed to explore the effects of the radius ratio  $\eta$  on turbulent Taylor-Couette flow. Numerical results corresponding to Taylor numbers in the range of  $10^4 < Ta < 10^8$  alongside with experiments in a Taylor number range of  $10^{10} < Ta < 10^{12}$  were presented for four values of the radius ratio  $\eta$ .

First the influence of the radius ratio on the global scaling laws  $Nu_\omega \sim Ta^\gamma$  was studied. The local scaling exponent  $\gamma$  describing the response of the torque caused by a Taylor number increase, is barely modified by varying the radius ratio  $\eta$ . Indeed, in experiments a universal exponent of  $\gamma \approx 0.39$  is obtained, independent of radius ratio and outer cylinder rotation. For the numerical simulations at lower  $Ta$  similar universal behavior can be observed. The transition associated to the vanishing of coherent structures can also be appreciated at  $Ta \sim 10^6$  for all values of  $\eta$ . Before this transition local exponents of  $\gamma \approx 0.33$  are seen and after the transition these decrease to about  $\gamma \approx 0.2$ .

The radius ratio does play a very important role in optimal transport. At smaller gaps, i.e., for larger  $\eta$ , at the lower end of the  $Ta$  range a very large increase in transport for corotating cylinders can be seen. The shift towards the asymptotic optimal transport happens in a much slower way for small gaps, but this shift is seen for all studied radius ratios. For the largest gap ( $\eta = 0.5$ ), optimal transport for pure inner cylinder rotation at the lowest drivings is obtained. The shift towards the asymptotic value happens suddenly, as two peaks can be seen in the  $Nu_\omega$  versus  $Ro^{-1}$  curve, and one of the peaks becomes

larger than the other one as driving increases. This might point in the direction of different phenomena happening at larger gaps. Finally, the asymptotic values of  $Ro_{opt}^{-1}$  obtained in experiments were compared to the speculations of van Gils *et al.* (2012) and Brauckmann & Eckhardt (2013*b*). Both of these speculations were found to deviate from experimental and numerical results.

When looking at the local results, as in Ostilla *et al.* (2013*b*) we can link the optimal transport in the smallest gaps to a balance between Coriolis forces and the inertia terms in the equations of motion. The flattest profiles in the bulk are linked to optimal transport in experiments. With the numerics the extrapolation presented in Ostilla *et al.* (2013*b*) for predicting optimal transport was extended to other radius ratios. It is found to work well for all selected  $\eta$  except for  $\eta = 0.5$ . At this  $\eta$ , i.e., for the largest gap considered here, the most obvious problem is that the  $\omega$  profiles strongly feel the effect of curvature difference at the inner and outer cylinders and a straight line fit to the bulk is not appropriate. There may be additional reasons for this discrepancy and optimal transport in large gaps requires more investigation.

Finally, the boundary layers have been analyzed. The outer boundary layer is found to be much thicker than the inner boundary layer when  $Ro^{-1} < Ro_{opt}^{-1}$ . We attribute this to the appearance of Rayleigh-stable zones in the flow. This prevents the rolls from covering the full domain between the cylinders. As the boundary layer size is essentially determined by the wind, if the rolls penetrate the whole domain (which is the case for  $Ro^{-1} > Ro_{opt}^{-1}$ ), both boundary layers are approximately of the same size. If the rolls do not penetrate the full domain, the outer boundary layer will be much larger than the inner boundary layer, in accordance with the smaller initial slope of  $\omega(r)$  at the cylinder walls.

In this work, simulations and experiments have been performed on a range of radius ratios between  $0.5 \leq \eta \leq 0.909$ . Insights for the small gaps seem to be consistent with what was discussed in Ostilla *et al.* (2013*b*). However, for  $\eta = 0.5$  the phenomena of optimal transport appears to be quite different. Therefore, our ambition is to extend the DNS towards values of  $\eta$  smaller than 0.5 to improve the understanding of that regime.

Acknowledgements: We would like to thank H. Brauckmann, B. Eckhardt, S. Merbold, M. Salewski, E. P. van der Poel and R. C. A. van der Veen for various stimulating discussions during these years. We acknowledge that the numerical results of this research have been achieved using the PRACE-2IP project (FP7 RI-283493) resource VIP based in Germany at Garching. We would also like to thank the Dutch Supercomputing Consortium SurfSARA for technical support and computing resources. We would like to thank FOM, COST from the EU and ERC for financial support through an Advanced Grant.

## REFERENCES

- AHLERS, G. 1974 Low temperature studies of the Rayleigh-Bénard instability and turbulence. *Phys. Rev. Lett.* **33**, 1185–1188.
- AHLERS, G., GROSSMANN, S. & LOHSE, D. 2009 Heat transfer and large scale dynamics in turbulent Rayleigh-Bénard convection. *Rev. Mod. Phys.* **81**, 503.
- ANDERECK, C. D., LIU, S. S. & SWINNEY, H. L. 1986 Flow regimes in a circular couette system with independently rotating cylinders. *J. Fluid Mech.* **164**, 155.
- BEHRINGER, R. P. 1985 Rayleigh-Bénard convection and turbulence in liquid-helium. *Rev. Mod. Phys.* **57**, 657 – 687.
- BODENSCHATZ, E., PESCH, W. & AHLERS, G. 2000 Recent developments in Rayleigh-Bénard convection. *Ann. Rev. Fluid Mech.* **32**, 709–778.
- BRAUCKMANN, H. & ECKHARDT, B. 2013*a* Direct numerical simulations of local and global torque in Taylor-Couette flow up to  $Re=30.000$ . *J. Fluid Mech.* **718**, 398–427.

- BRAUCKMANN, H. & ECKHARDT, B. 2013*b* Intermittent boundary layers and torque maxima in Taylor-Couette flow. *Phys. Rev. E* **87**, 033004.
- BUSSE, F. H. 1967 The stability of finite amplitude cellular convection and its relation to an extremum principle. *J. Fluid Mech.* **30**, 625–649.
- CHANDRASEKHAR, S. 1981 *Hydrodynamic and Hydromagnetic Stability*. New York: Dover.
- COUGHLIN, K. & MARCUS, P. S. 1996 Turbulent bursts in Couette-Taylor flow. *Phys. Rev. Lett.* **77** (11), 2214–17.
- CROSS, M. C. & HOHENBERG, P. C. 1993 Pattern formation outside of equilibrium. *Rev. Mod. Phys.* **65** (3), 851.
- DOMINGUEZ-LERMA, M. A., CANNELL, D. S. & AHLERS, G. 1986 Eckhaus boundary and wavenumber selection in rotating Couette-Taylor flow. *Phys. Rev. A* **34**, 4956.
- DONG, S 2007 Direct numerical simulation of turbulent Taylor-Couette flow. *J. Fluid Mech.* **587**, 373–393.
- DONG, S 2008 Turbulent flow between counter-rotating concentric cylinders: a direct numerical simulation study. *J. Fluid Mech.* **615**, 371–399.
- DRAZIN, P.G. & REID, W. H. 1981 *Hydrodynamic stability*. Cambridge: Cambridge University Press.
- ECKHARDT, B., SCHNEIDER, T.M., HOF, B. & WESTERWEEEL, J. 2007 Turbulence transition in pipe flow. *Annu. Rev. Fluid Mech.* **39**, 447–468.
- FASEL, H. & BOOZ, O. 1984 Numerical investigation of supercritical Taylor-vortex flow for a wide gap. *J. Fluid Mech.* **138**, 21–52.
- GEBHARDT, TH. & GROSSMANN, S. 1993 The Taylor-Couette eigenvalue problem with independently rotating cylinders. *Z. Phys. B* **90** (4), 475–490.
- VAN GILS, D. P. M., BRUGGERT, G. W., LATHROP, D. P., SUN, C. & LOHSE, D. 2011*a* The Twente Turbulent Taylor-Couette ( $T^3C$ ) facility: strongly turbulent (multi-phase) flow between independently rotating cylinders. *Rev. Sci. Instr.* **82**, 025105.
- VAN GILS, D. P. M., HUISMAN, S. G., BRUGGERT, G. W., SUN, C. & LOHSE, D. 2011*b* Torque scaling in turbulent Taylor-Couette flow with co- and counter-rotating cylinders. *Phys. Rev. Lett.* **106**, 024502.
- VAN GILS, D. P. M., HUISMAN, S. G., GROSSMANN, S., SUN, C. & LOHSE, D. 2012 Optimal Taylor-Couette turbulence. *J. Fluid Mech.* **706**, 118.
- GROSSMANN, S. & LOHSE, D. 2000 Scaling in thermal convection: A unifying view. *J. Fluid. Mech.* **407**, 27–56.
- GROSSMANN, S. & LOHSE, D. 2001 Thermal convection for large Prandtl number. *Phys. Rev. Lett.* **86**, 3316–3319.
- GROSSMANN, S. & LOHSE, D. 2011 Multiple scaling in the ultimate regime of thermal convection. *Phys. Fluids* **23**, 045108.
- GROSSMANN, S. & LOHSE, D. 2012 Logarithmic temperature profiles in the ultimate regime of thermal convection. *Phys. Fluids* **24**, 125103.
- HEISE, M., HOFFMANN, CH., WILL, CH., ALTMAYER, S., ABSHAGEN, J. & PFISTER, G. 2013 Co-rotating Taylor-Couette flow enclosed by stationary disks. *J. Fluid Mech.* **716** (R4).
- HUISMAN, S.G., VAN GILS, D.P.M. & SUN, C. 2012*a* Applying laser doppler anemometry inside a Taylor-Couette geometry – using a ray-tracer to correct for curvature effects. *Eur. J. Mech. - B/Fluids* .
- HUISMAN, S. G., VAN GILS, D. P. M., GROSSMANN, S., SUN, C. & LOHSE, D. 2012*b* Ultimate turbulent Taylor-Couette flow. *Phys. Rev. Lett.* **108**, 024501.
- HUISMAN, S. G., SCHARNOWSKI, S., CIERPKA, C., KAEHLER, C., LOHSE, D. & SUN, C. 2013 Logarithmic boundary layers in highly turbulent Taylor-Couette flow. *Phys. Rev. Lett* **submitted**.
- KADANOFF, L. P. 2001 Turbulent heat flow: Structures and scaling. *Phys. Today* **54** (8), 34–39.
- LATHROP, D. P., FINEBERG, JAY & SWINNEY, H. S. 1992*a* Transition to shear-driven turbulence in Couette-Taylor flow. *Phys. Rev. A* **46**, 6390–6405.
- LATHROP, D. P., FINEBERG, JAY & SWINNEY, H. S. 1992*b* Turbulent flow between concentric rotating cylinders at large Reynolds numbers. *Phys. Rev. Lett.* **68**, 1515–1518.
- LEWIS, G. S. & SWINNEY, H. L. 1999 Velocity structure functions, scaling, and transitions in high-Reynolds-number Couette-Taylor flow. *Phys. Rev. E* **59**, 5457–5467.

- LOHSE, D. & XIA, K.-Q. 2010 Small-scale properties of turbulent Rayleigh-Bénard convection. *Ann. Rev. Fluid Mech.* **42**, 335–364.
- LORENZ, E. N. 1963 Deterministic nonperiodic flow. *J. Atmos. Sci.* **20**, 130–141.
- MERBOLD, S., BRAUCKMANN, H. & EGBERS, C. 2013 Torque measurements and numerical determination in differentially rotating wide gap Taylor-Couette flow. *Phys. Rev. E* **87**, 023014.
- OSTILLA, R., VAN DER POEL, E., VERZICCO, R. & LOHSE, D. 2013a Transition between the classical and ultimate regimes of Taylor-Couette flow: a novel viewpoint based on boundary layer-bulk interactions. *to be submitted*.
- OSTILLA, R., STEVENS, R. J. A. M., GROSSMANN, S., VERZICCO, R. & LOHSE, D. 2013b Optimal Taylor-Couette flow: direct numerical simulations. *J. Fluid Mech.* **719**, 14–46.
- PAOLETTI, M. S. & LATHROP, D. P. 2011 Angular momentum transport in turbulent flow between independently rotating cylinders. *Phys. Rev. Lett.* **106**, 024501.
- PFISTER, G. & REHBERG, I. 1981 Space dependent order parameter in circular Couette flow transitions. *Phys. Lett.* **83**, 19–22.
- PFISTER, G., SCHMIDT, H., CLIFFE, K. A. & MULLIN, T. 1988 Bifurcation phenomena in Taylor-Couette flow in a very short annulus. *J. Fluid Mech.* **191**, 1–18.
- PIRRO, DAVIDE & QUADRIO, MAURIZIO 2008 Direct numerical simulation of turbulent Taylor-Couette flow. *Eur. J. Mech. B-Fluids* **27**, 552.
- SIGGIA, E. D. 1994 High Rayleigh number convection. *Annu. Rev. Fluid Mech.* **26**, 137–168.
- SMITH, G. P. & TOWNSEND, A. A. 1982 Turbulent Couette flow between concentric cylinders at large Taylor numbers. *J. Fluid Mech.* **123**, 187–217.
- STEVENS, R. J. A. M., LOHSE, D. & VERZICCO, R. 2011 Prandtl and Rayleigh number dependence of heat transport in high Rayleigh number thermal convection. *J. Fluid Mech.* **688**, 31–43, submitted.
- STEVENS, R. J. A. M., VERZICCO, R. & LOHSE, D. 2010 Radial boundary layer structure and Nusselt number in Rayleigh-Bénard convection. *J. Fluid Mech.* **643**, 495–507.
- STROGATZ, S. H. 1994 *Nonlinear dynamics and chaos*. Reading: Perseus Press.
- TAYLOR, G. I. 1936 Fluid friction between rotating cylinders. *Proc. R. Soc. London A* **157**, 546–564.
- TONG, P., GOLDBURG, W. I., HUANG, J. S. & WITTEN, T. A. 1990 Anisotropy in turbulent drag reduction. *Phys. Rev. Lett.* **65**, 2780–2783.
- VERZICCO, R. & ORLANDI, P. 1996 A finite-difference scheme for three-dimensional incompressible flow in cylindrical coordinates. *J. Comput. Phys.* **123**, 402–413.
- WENDT, F. 1933 Turbulente Strömungen zwischen zwei rotierenden Zylindern. *Ingenieurs-Archiv* **4**, 577–595.
- XIA, K.-Q., LAM, S. & ZHOU, S. Q. 2002 Heat-flux measurement in high-Prandtl-number turbulent Rayleigh-Bénard convection. *Phys. Rev. Lett.* **88**, 064501.